Measuring high-resolution sky luminance distributions with a CCD camera

Korntip Tohsing,* Michael Schrempf, Stefan Riechelmann, Holger Schilke, and Gunther Seckmeyer

Institut für Meteorologie und Klimatologie, Leibniz Universität Hannover, Herrenhäuser Strasse 2, Hannover 30419, Germany

*Corresponding author: tohsing@muk.uni-hannover.de

We describe how sky luminance can be derived from a newly developed hemispherical sky imager (HSI) system. The system contains a commercial compact charge coupled device (CCD) camera equipped with a fish-eye lens. The projection of the camera system has been found to be nearly equidistant. The luminance from the high dynamic range images has been calculated and then validated with luminance data measured by a CCD array spectroradiometer. The deviation between both datasets is less than 10% for cloudless and completely overcast skies, and differs by no more than 20% for all sky conditions. The global illuminance derived from the HSI pictures deviates by less than 5% and 20% under cloudless and cloudy skies for solar zenith angles less than 80°, respectively. This system is therefore capable of measuring sky luminance with the high spatial and temporal resolution of more than a million pixels and every 20 s respectively.   © 2013 Optical Society of America

OCIS codes: 120.0120, 000.2190.

1. Introduction

Solar radiation is the Earth's main source of energy. Radiation of wavelengths between approximately 380 and 780 nm is defined as visible radiation [1]. This part of the solar spectrum is visible to the human eye and plays a great role for our daily life. Often artificial light is used to compensate for a lack of proper illumination inside buildings. Typically modern building designs include stronger considerations of daylight utilization due to the energy saving potential [2,3] and positive effects on the human psyche [4,5]. Therefore, the knowledge of sky luminance distribution is an important input quantity to use daylight in buildings efficiently. In addition, luminance data is not only useful for daylight applications but also for risk assessment of the eye exposure to blue light of visible radiation for outdoor activities [6].

The luminance is defined as the luminous flux per unit solid angle emitted from a surface element in a given direction, per unit area measured in cd/m² [7]. As a result of the importance of luminance data, monitoring stations have been established where luminance is routinely measured [8]. However, instruments that are capable of measuring luminance are costly due to the need of scanning components, and the number of stations performing luminance measurements is therefore limited. Thus, many researchers have developed models to determine the sky luminance distribution for different weather conditions [9–14].

The wide use of digital charge coupled device (CCD) cameras during the last 10 yr has led to an increased use of cameras in scientific investigations. Acquiring high spatial resolution images and analyzing them in near real time has become possible. We developed a hemispherical sky imager (HSI) system based on a commercial CCD camera to obtain a variety of sky properties, such as sky luminance, sky radiance, and cloud cover. Similar imaging systems have been

successfully used to retrieve information on cloud cover and have also been validated with synoptic observations [15–18]. A relationship between digital count values of the red and blue channels of hemispherical images named sky index was defined to derive cloud cover [19]. In [20], a fully automatic cloud classification from digital images for seven different sky conditions was proposed. The aerosol and cloud optical depth at 550 nm from sky images has been derived by using the Santa Barbara DISORT Atmospheric Radiative Transfer model [21]. The utilization of sky imagery is not only suitable for the determination of several cloud parameters but may also be applied to derive photometric and radiometric quantities. Gray levels of the electro-optic fish-eye radiance distribution camera system have been applied for measured radiance distribution and the calibration of the system was also presented [22]. In [23], a monochromatic CCD camera has been used to derive the sky radiance distributions and sky luminance distributions for different sky conditions. The color images applied for spectral radiance at the central wavelength and the calibration method was proposed [24]. In [25], the luminance distribution measured by a color CCD camera was evaluated. The RGB components of the pictures were used to obtain the related luminance function. However, the dynamic range of these pictures was quite limited and the method is not generally applicable. Furthermore, the data were not evaluated against other luminance measurements.

In this paper, we demonstrate how a sky imagery system that provides hemispherical images can be used to measure sky luminance. An experimental setup is designed to determine the projection of this fish-eye lens of the camera and some brighter stars of night images were used as reference points to check the geometry calibration. The RGB values of high dynamic range (HDR) images, including the camera metadata from images, were employed to derive the sky luminance. Finally, a comparison between the camera-based and measured sky luminance for different sky conditions is presented. In addition, the global illuminance derived from the HSI system is evaluated with data measured by a luxmeter.

2. Instruments and Methods

A. Instruments

1. Hemispherical Sky Imager
The HSI was developed and installed on the roof of the Institute of Meteorology and Climatology (IMuK), University of Hannover, Germany, 52.39°N, 9.70°E, at 59 m above sea level. This system contains a Canon PowerShot G10 camera, equipped with a Dörr DHG fish-eye lens, providing a field of view (FOV) of about 183°. The sensor of the camera is a 1/1.7″ CCD chip (7.6 × 5.7 mm) with a maximum image size of 4416 × 3312 pixels (corresponding to 3.5 million pixels for the hemispherical image with a radius of 1060 pixels). Due to the green masked areas of the Bayer filter on the chip the spatial resolution corresponds to about 1.7 million pixels. The analogue digital converter (ADC) of the camera has 8 bits of resolution, which equals to 256 counts per pixel. The file format is JPEG and the information is saved as RGB values. Images are taken every 20 s by using autobracketing function for three shutter speeds, such as 0.0005, 0.001, and 0.002 s but the ISO number and the f-stop are kept constant as ISO 80 and $f/4.0$, respectively. A weatherproof camera housing has been designed to provide long-term outside operation. The alignment of the HSI system has been carefully treated. The deviation of the vertical alignment and the north alignment of the system are within $\pm 2°$.

2. CCD Spectroradiometer
A CCD spectroradiometer system based on an CCD array spectrometer (S2000, Ocean Optics Inc., Dunedin, USA) and a positioning unit is used for the validation of the HSI system. The CCD spectroradiometer provides spectral sky radiance, which is converted to sky luminance according to Eq. (1). Similar spectrometers have been used to measure solar and artificial radiation in [26–29]. The system is capable of measuring spectral sky radiance with a spectral resolution of 2 nm between 300 and 800 nm covering the visible part of the spectrum used to calculate sky luminance. The positioning unit has entrance optics with a 5° FOV [30]. The spectral sky radiance at a given zenith and azimuth angles is measured within 5 s. The system is further denoted as CCD spectroradiometer. Based on earlier investigations with the main focus on the UV range, we estimate the uncertainty of the spectral radiance measurements between 5% and 10%. The methodology for the calibrations used for this study are described in more detail in Pissulla *et al.* [31] and in Seckmeyer *et al.* [30] has been applied to spectral radiance measurements in the visible. The effects of uncertainties on experimental integrals (like the luminance) have been described in Cordero *et al.* [32], and further details on the extension to the visible range can be found in Wuttke and Seckmeyer [33] and Wuttke *et al.* [34]. The general methods for uncertainty evaluation have been described in Bernhard and Seckmeyer [35] and in Cordero *et al.* [36]. A calibration of the CCD spectroradiometer has been performed according to [31] at the beginning of the measurement campaign.

3. Luxmeter
A luxmeter is used for checking the results of the HSI system over longer time periods. Illuminance is defined as photometric flux per unit area, which can be calculated by integrating visible solar spectral irradiance weighted by the response of the human eye over the wavelength [37]. The definitions of some photometric and radiometric quantities are listed in the Table 1 [38]. A temperature stabilized luxmeter provides the highly accurate illuminance measurement in the range of 0.001 lux to 200 klux [39]. This

Table 1. Definition of Radiometric (Radiance, Irradiance) and Photometric (Luminance, Illuminance) Quantities According to [38]

Quantity	Definition	Formula	SI Unit
Radiance	Ratio of the radiant flux $d\Phi_e$ transmitted by an elementary beam passing through the given point and the propagating in the solid angle $d\Omega$ and the area of a section of that beam containing the given point dA. θ is the angle between the normal to that section and the direction of the beam.	$L_e = d\Phi_e/(dA \cdot \cos\theta \cdot d\Omega)$	$\mathrm{W\,m^{-2}\,sr^{-1}}$
Irradiance	Ratio of the radiance flux $d\Phi_e$ incident on an element of the surface containing the point, by the area dA of that element.	$E_e = d\Phi_e/dA$	$\mathrm{W\,m^{-2}}$
Luminance	Ratio of the luminous flux $d\Phi_v$ transmitted by an elementary beam passing through the given point and the propagating in the solid angle $d\Omega$ and the area of a section of that beam containing the given point dA. θ is the angle between the normal to that section and the direction of the beam.	$L_v = d\Phi_v/(dA \cdot \cos\theta \cdot d\Omega)$	$\mathrm{cd\,m^{-2}}$
Illuminance	Ratio of the luminous flux $d\Phi_v$ incident on an element of the surface containing the point, by the area dA of that element.	$E_v = d\Phi_v/dA$	$\mathrm{lm\,m^{-2}}$

luxmeter was used in the investigation and measurement of the global illuminance within 1 min intervals.

B. Methods

1. Camera Projection Function Determination

In order to calculate luminance from different sky directions, the relation between the zenith angle of the sky position and the position of the pixel on the image needs to be determined. For taking whole sky images, the hemisphere is mapped by a projection function onto a two-dimensional image. A projection function is described as a relation between the angle (α) of the incoming light beam and the distance (r) of the optical axis from the center of the image. There are three projection functions commonly used for large FOV objectives:

$$r = c \cdot \alpha \quad \text{(Equidistant projection)},$$

$$r = 2c \cdot \sin\frac{\alpha}{2} \quad \text{(Equisolid-angle projection)},$$

$$r = c \cdot \sin\alpha \quad \text{(Orthographic projection)},$$

where c is the focal length [40].

To analyze all-sky images correctly and to determine cloud parameters like cloud cover or cloud type and photometric quantities like sky luminance the knowledge of the projection function of the camera system is essential. The characterization of the projection function has been performed by an experimental setup called a camera distortion determination, as shown in Fig. 1(a). A semicircle has been labeled with zenith angles and represents the hemisphere. By taking an image of the setup in direction of the zenith, each label was assigned to an associated image pixel. The radius and zenith angle of each label has been analyzed and the result of the characterization for this camera system will be presented in Subsection 3.A.

For the validation of a projection function, a calibration based on star positions was also applied. Nighttime images were taken every 5 min on April 19, 2010 with an exposure time of 15 s. As an example, an image at 21.55 UTC is shown in Fig. 1(b). 18 stars with an apparent magnitude brighter than 2.50 magnitudes could be identified. The corresponding zenith and azimuth angles of the stars were calculated by the astronomic software package Stellarium
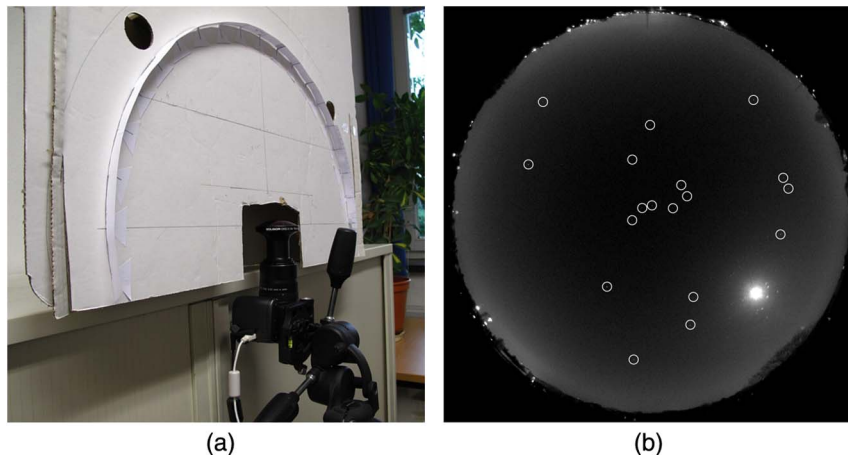

(a) (b)

Fig. 1. (Color online) Image (a) shows the setup for the camera distortion determination and (b) shows an image of the nighttime sky taken on April 19th, 2010 at 21.55 UTC with an exposure time of 15 s. Despite the fact that the horizon is light contaminated by street illumination and the moon can clearly be recognized in the picture, 18 bright stars (marked with circles) could be identified and are used for the star calibration.

[41]. The relation between the positions of the stars and their zenith angles was then determined. By this method our previous determination is validated, as discussed in Subsection 3.A.

2. High Dynamic Range Acquisitions

Due to the large dynamic range of the sky radiance, the 8 bit ADC of the camera provides not enough resolution to capture the sky radiance in sufficient detail. The luminance determined by the HSI system using only one exposure image or low dynamic range has a dynamic range of only about 3 orders of magnitude and the saturation at the circumsolar region or from bright clouds causes a deviation of the luminance calculation. Therefore, to increase the dynamic range of the HSI system, an HDR image is composed of three images with different exposure times of the same scene [42,43]. Each pixel of the HDR image has about 0.085° FOV, thus ~60 × 60 pixels correspond to the 5° FOV of the CCD spectroradiometer. Nevertheless, it is not possible to capture pictures in situations with direct sunlight without saturation of the image of the solar disc. Therefore, we exclude the solar disc region and a part of the circumsolar region of approximately 10° in diameter.

3. Conversion of Radiance to Luminance

Spectral radiance can be converted to luminance by the following formula [44]:

$$L_{ph} = K_m \int_{380}^{780} R(\lambda) \cdot V(\lambda) d\lambda, \qquad (1)$$

where L_{ph} is the luminance in cd/m², K_m of 683 lm/W is the conversion constant, and $V(\lambda)$ is the daylight spectral response of the human eye. $R(\lambda)$ is the spectral radiance in W/(m² nm sr) and its definition is presented in the Table 1.

4. Luminance from All-Sky Images

The luminance from the all-sky images was derived from the RGB pixel values, shutter speed, f-stop number, and ISO number by applying the following Eqs. (2)–(4) based on the equations of Roy et al. [25]:

$$L_{cam} = \frac{V^{a_T}}{b_T \cdot E_v}, \qquad (2)$$

$$V = 0.2125R + 0.7154G + 0.0721B, \qquad (3)$$

$$E_v = \frac{179}{200} \cdot \pi \cdot S \cdot \frac{T}{f^2}, \qquad (4)$$

where L_{cam} is the luminance of the sky for each pixel in cd/m². V is the luminance function calculated from the RGB values of an all-sky image, which range from 0 to 255. E_v is the exposure value, which describes the relation between the shutter speed (T) in second, the f-stop number f, and the ISO number S. The power a_T and factor b_T were determined by an experimental investigation in the laboratory as follows. In contrast to Roy et al. [25], who are using only a constant for a_T and do not introduce b_T, we evaluated a_T and b_T by measuring luminance as described below.

The calibration was performed on a calibration bar in a temperature stabilized lab room with blackened walls and with a suitable baffle setup to reduce stray light during the calibration process (Pissulla et al. [31]). As presented in Fig. 2, a reflectance plaque was illuminated by a 1000 W tungsten halogen lamp, which has been calibrated by the Physikalisch–Technische Bundesanstalt, a national metrology institute. The uncertainty of the irradiance is about ±1% for the wavelength region from 400 to 780 nm. The lamp is controlled by a stabilized power source. By means of a calibrated shunt the power is stabilized to 8 ± 0.0001 A. Details of this calibration method are described in Pissulla et al. [31]. The reflectance of the plaque is >98% in the wavelength region from 380 to 780 nm. The plaque was centered in the FOV of the camera in a distance of 35 cm from the lamp. During the calibration process the distance has been increased in intervals of 5 cm up to 565 cm.
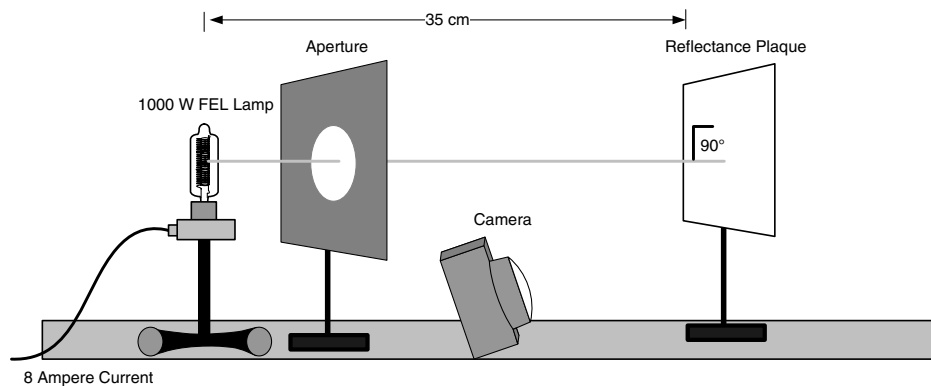

Fig. 2. Reflectance plaque is illuminated perpendicularly by a 1000 W tungsten halogen lamp. The plaque provides uniform radiance for the luminance calibration in the center of the HSI image. Images of the plaque were acquired with different exposure times varied from 1/2000 s to 1/20 s.

At each position images of the plaque were acquired with constant ISO number and aperture and for 21 exposure times from 1/2000 s to 1/20 s (Fig. 3). The spectral radiance emitted from the plaque at each position is converted to luminance by applying Eq. (1). To calibrate the HSI the luminance calculated by Eqs. (2)–(4) shall agree with the luminance emitted by the plaque. This is achieved by varying the parameters a_T and b_T for each exposure time. Repeated calibrations gave consistent results. The luminance of each pixel of an HDR image is calculated in dependence of its corresponding exposure time.

5. Quality Control of Luminance Data

The illuminance has been calculated from luminance data of the sky radiance in addition to calculation of the direct illuminance. These data have been intercompared with data from a luxmeter. The diffuse illuminance is calculated by the following equation [45]:

$$E_{\mathrm{dh}} = \int_0^{2\pi} \int_0^{\pi/2} L_{\gamma,\varphi} \sin \gamma \, \cos \gamma \mathrm{d}\gamma \mathrm{d}\varphi, \qquad (5)$$

where E_{dh} is the diffuse illuminance on the horizontal plane (lm/m² or lux) and $L_{\gamma,\varphi}$ is the luminance of the point on the sky with the corresponding elevation angle (γ) and azimuth angle (φ).

Under cloudless skies the main contribution to the global illuminance is the direct component from the sun. The direct illuminance of the sunlight is obtained from the Eq. (6) proposed by Krochmann and Seidl [11]:

$$E_s = 130 \cdot \sin \gamma_s \cdot \exp(-0.2/\sin \gamma_s), \qquad (6)$$

where E_s is direct illuminance from the sun in klux and γ_s is solar elevation angle in degrees.

The global illuminance is calculated by summing the direct illuminance [Eq. (6)] and the diffuse illuminance [Eq. (5)] from the camera, if the sun is not obscured by clouds; otherwise, the direct illuminance is set to zero.

The comparison of global illuminance is only a rough quality check since under direct sunlight only the diffuse illuminance is measured by the HSI. In this case, the major part of the global illuminance is calculated with a parameterized formula that is mainly dependent of the solar elevation angle and has no aerosol optical depth dependence. This check might therefore not work with higher aerosol contents than those present during the two months of our evaluation campaign.

3. Results

A. Camera Projection Function

The deviation of the camera projection compared to an equidistant projection has been characterized in the lab performing a camera distortion determination (Fig. 1) and in the field performing a star calibration according to Subsection 2.B.1. The relation between a radial distance from the image center and the zenith angle of the stars is nearly linear, as shown in Fig. 4, and is fitted by the following equation:

$$r_i = 0.0187683 + 0.0196850 \cdot \theta_i, \qquad (7)$$

where θ is the zenith angle in degrees and i is the pixel number of the image. The R^2 coefficient of correlation is 0.998. The transformation of zenith and azimuth angle to image coordinates can be performed using Eqs. (8) and (9):

$$x_i = x_0 + r_i(\theta_i) \cdot \cos(\varphi_i), \qquad (8)$$

$$y_i = y_0 + r_i(\theta_i) \cdot \sin(\varphi_i), \qquad (9)$$

where x_i, y_i are the pixels of the image and x_0, y_0 the centers of the image. θ_i is the zenith angle with $0 \leq \theta_i \leq 90°$ and φ_i is azimuth angle with $0 \leq \varphi_i \leq 360°$.
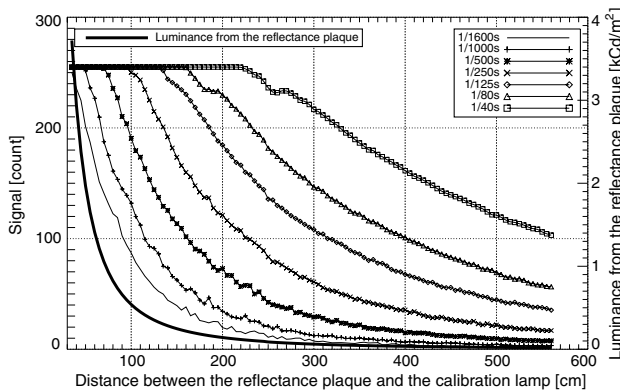

Fig. 3. Counts (left axis) of the red channel measured during the luminance calibration for seven different exposure times as a function of the distance between the reflectance plaque and the calibration lamp. The black solid line represents the luminance (right axis) emitted by the reflectance plaque.
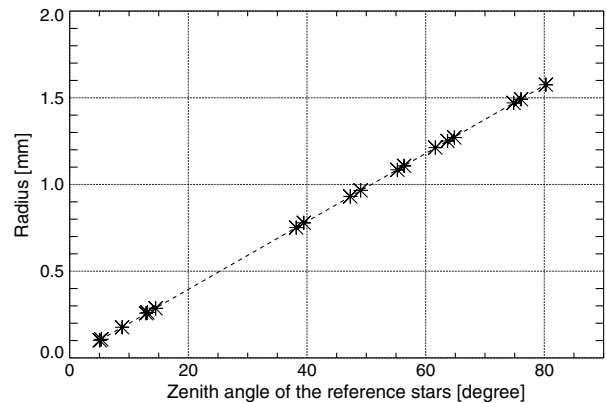

Fig. 4. Radial distance from optical axis to image center or zenith point, r in millimeter and zenith angle of the 18 reference stars with the square of correlation coefficient (R^2) of 0.998.
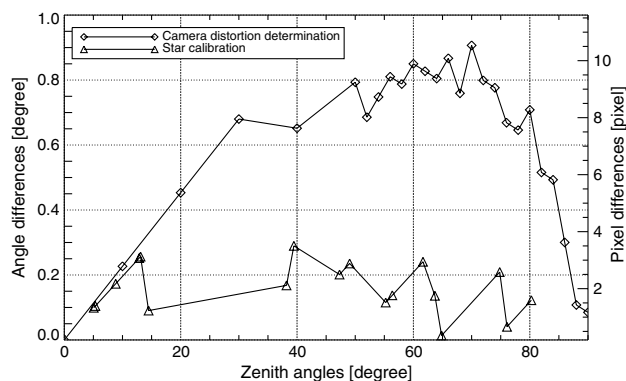
Fig. 5. Deviation of different measurements to the equidistant geometry determined in degrees (left axis) and pixels (right axis) for the camera distortion determination (diamond) and star calibration (triangle). Both calibration methods agree well with the equidistant geometry.

The deviation of the camera projection derived with the camera distortion determination and the star calibration compared to the equidistant projection are presented in Fig. 5. The derived projection functions agree well within 1° compared to the equidistant projection function. The uncertainty of the measurement for the star calibration is within 5 pixels or about 0.4°, whereas the camera distortion determination has an uncertainty of 10 pixels or 0.9°. We conclude that the used fish-eye objective provides a nearly equidistant projection function, which is used for the luminance calculations.

B. Comparison of Luminance Distribution between HSI and CCD Spectroradiometer

For the validation of the calibration method, the diurnal zenith luminance measured with the CCD spectroradiometer has been compared with the diurnal sky luminance of HSI images. Figure 6 shows a comparison between measured and computed zenith luminance. March 28th 2012 was a nearly cloudless day with few cirrus clouds before 8.00 UTC (a). May 12th 2012 was a day with broken cloud conditions (c). The black line and gray line show the zenith luminance from CCD and HSI system, respectively. The ratio of the camera-based zenith luminance to measured zenith luminance is presented in plots (b) and (d) for both days, respectively. Figure 6(e) shows the corresponding HSI image taken on May 12th 2012 at 15.31 UTC. The black circle indicates the zenithal position of the image corresponding to the FOV of the CCD spectroradiometer. The deviation of zenith luminance for clear sky on March 28th derived from HDR images compared to the CCD spectroradiometer is less than 10%. With clouds, especially cirrus clouds, as shown in Fig. 6(e) the zenith luminance drastically changed and the ratio of instantaneous zenith luminance from HDR images to the CCD spectroradiometer can be up to a factor of 2. We assume that this short-time variation is mainly caused by a synchronization problem. While the measurements of the CCD spectroradiometer

are acquired in 1 s the HDR images of the HSI system are captured in approximately 3 s. Time asynchrony of both measuring PCs may cause an additional asynchrony of 1 s. In case of fast moving clouds this results in the observed deviation between both instruments. In addition, the deviation of the hourly averaged measured and camera-based zenith luminance for clear sky (March 28th) and overcast sky (February 13th) is less than 10%. Hourly averages during broken cloud conditions (May 12th) lead to a deviation of less than 20%.

The daily averaged (4.00 UTC–18 UTC) zenith luminance from CCD spectroradiometer and HSI images from different dates in February–May 2012, which contain various weather conditions, were also compared, as shown in Fig. 7(a). The ratio of calculated daily zenith luminance to CCD spectroradiometer is shown in Fig. 7(b). The deviation of daily average zenith luminance from HDR images for homogenous skies (cloudless and overcast skies) is mostly less than 10% and up to 20% for the partly cloudy sky condition.

To verify whether the calibration method is applicable for luminance calculation within the whole sky hemisphere, the daily averaged luminance derived from HDR images for different sky elements with corresponding zenith angles of 36° and 60° was also compared with the luminance from CCD spectroradiometer. The deviation is found to be less than 10% for clear sky condition (March 28th 2012), whereas in the case of partly cloudy sky (May 12th 2012) the difference was up to 20%.

C. Comparison of Global Illuminance between HSI and Luxmeter

A time series of global illuminance from the luxmeter and camera-based measurements with 1 min interval and the corresponding ratios are plotted in Fig. 8. Global illuminance derived from HSI images from March 28th 2012 under clear sky conditions (upper panel) show a good agreement with the data from the luxmeter. The deviation lies within 5% for zenith angle less than 80°. For a cloudy situation (lower panel) on May 12th 2012, the (c) shows the extreme variation of illuminance only from luxmeter data due to broken cloud conditions during that day. The ratio of the comparison (d) shows a large deviation between the HSI and the luxmeter. The maximum deviation of instantaneous HSI data can vary within 40% due to small synchronization differences, which can deviate up to 5 s between the HSI system and the luxmeter. Global illuminance from HDR calculation is often smaller than the measurement because cumulus clouds enhance solar radiation at circumsolar region by 25%. In this case the calculation from all-sky images can hardly resolve such a complex situation. The global illuminance evaluation shown in Fig. 8 can be implied as the approximately check for the sky luminance from the HSI system because of the most contribution of the direct illuminance, about 80% which was obtained from the model
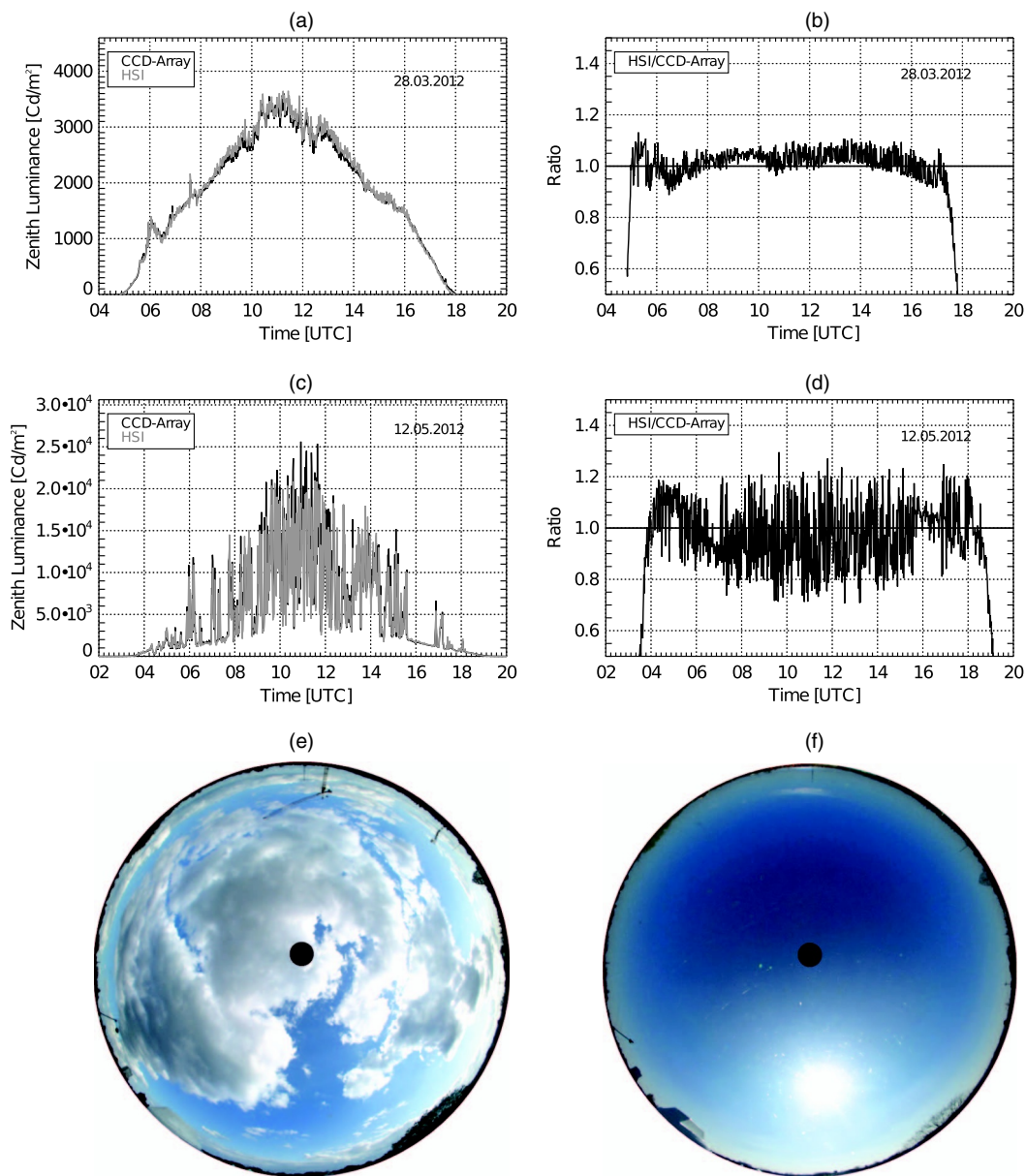
Fig. 6. (a)–(d) Diurnal variation of zenith sky luminance measured with CCD spectroradiometer (black line) and HSI (gray line). (a) Comparison of zenith sky luminance on March 28th 2012 under clear sky conditions and (b) the corresponding ratio. (c) Comparison of zenith sky luminance on May 12th 2012 for broken cloud conditions and (d) the corresponding ratio. (e) HSI image for a broken cloud condition from May 12th 2012 at 15:31 UTC and (f) HSI image of a clear sky condition from March 28th 2012 at 11:50 UTC. The black circles on the images (e) and (f) mark the corresponding FOV of the CCD spectroradiometer entrance optics. The sky luminance in the morning is only 1% of the noon sky luminance. The figure shows that the deviation between both measurements is less than ±10% for these instantaneous measurements that are not averaged.

described in [11]. Therefore, the global illuminance for overcast or homogeneous sky without influencing of the direct illuminance has been analyzed for February 13th 2012. The diurnal variation on this day was within 10%. The daily averaged (4.00 UTC–18 UTC) of global illuminance from HDR images in May 2012 shows also a good agreement with measurements from the luxmeter with a deviation of less than 10%, as shown in Fig. 9. In general, it can be concluded that the deviation of global illuminance from HDR images and luxmeter measurement can be up to 20% for all weather conditions.

4. Remarks and Discussion

• The temperature of the HSI camera inside the housing varies between 10°C and 35°C. However, due to the heating and ventilation of the camera housing we estimate the temperature of the camera sensor to be 20 ± 5°C. The typical sensitivity variation of a CCD camera sensor is 0.3% per Kelvin according to [46,47]. Within the usual range of the temperatures this results in a corresponding uncertainty of 3% and can therefore be considered small compared to other uncertainties.
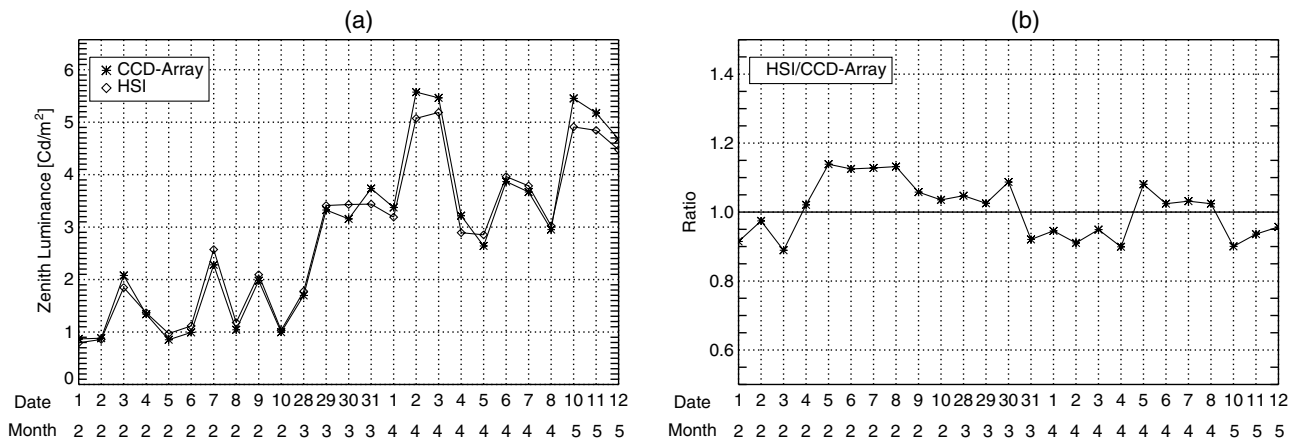
Fig. 7. (a) Daily averaged zenith luminance measured by the CCD spectroradiometer (star) compared with HSI (diamond) calculation on different dates in February–May 2012. (b) Ratio of daily averaged zenith luminance derived from HSI images to the measurement of CCD spectroradiometer.
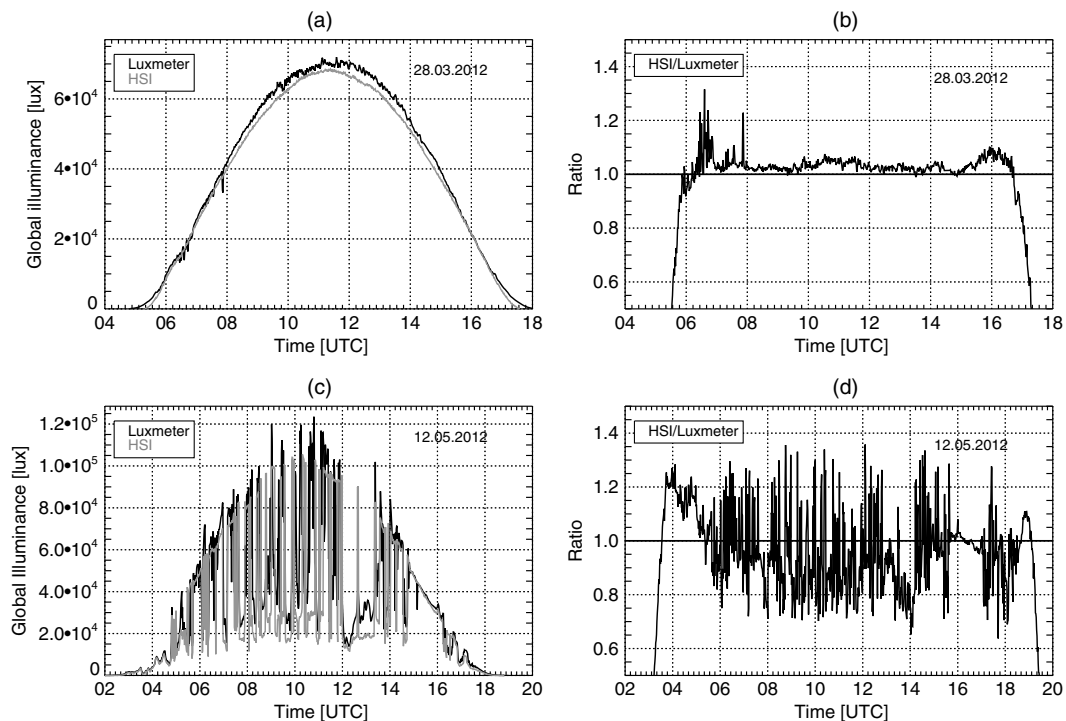

Fig. 8. Diurnal variation of global illuminance on (a) March 28th and (c) May 12th 2012. Plot (a) shows the comparisons between the measured illuminance from the luxmeter (black line) and the illuminance derived from the HSI system (gray line) on March 28th. Plot (c) presents the illuminance from the luxmeter on May 12th 2012. The corresponding ratios of HSI's illuminance to illuminance from the luxmeter for both days are shown in plots (b) and (d).

• The HSI system is operational both in shade and direct sunlight [Figs. 6(e) and 6(f)]. Internal reflections may occur in the images under direct sunlight. These ghost images depend on the solar position and therefore affect different areas of the image. However, an investigation of ghost images has shown that less than 2% of the image is affected and cannot be used for the luminance calculation. Ghost images can additionally be detected to a large extent by algorithms, due to their well-defined edges.

• Stray light that might originate from other sources like reflections on the walls of the lens tube of the fish-eye objective has not yet been fully characterized. However, the comparison between the HSI and the CCD spectroradiometer in Subsection 3.B showed that stray light effects cannot be severe.

• The camera has likely some kind of automatic offset correction but sporadic hot pixel could be observed. Those outliers have not yet been eliminated.
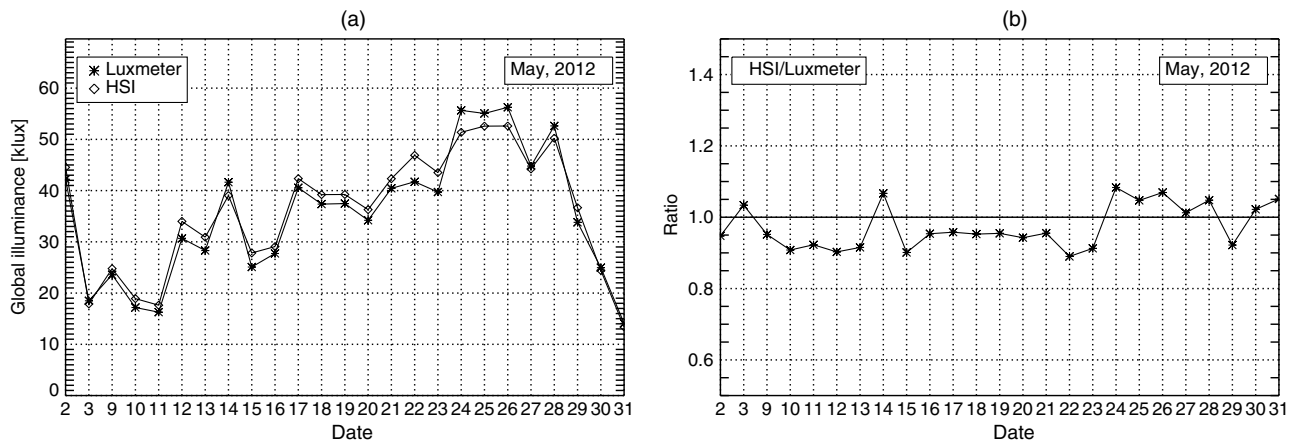
Fig. 9. (a) Comparison between daily averaged global illuminance measured from the luxmeter (star) and HSI (diamond) calculation on different dates in May 2012. (b) Ratio of daily average global illuminance from HSI images to the measured values from the luxmeter.

• No investigations concerning roll-off properties of the fish-eye objective, sensor noise, and sensor uniformity have been performed yet. The camera was used with the automatic color balance (white balance) provided by the manufacturer. The effect of this automatic procedure on the luminance determination is not exactly known. However, these missing characterizations appear to have little impact on the luminance determination since the instrument comparisons did not indicate any severe problems.

5. Conclusion

A compact CCD camera system equipped with a fish-eye lens for photometric observations has been presented. An experimental setup to examine the geometric fish-eye projection and a validation of this calibration using the stars as reference points has been performed and compared with other camera projections. The projection function of the camera system can be well approximated by an equidistant projection. Sky luminance has been derived from hemispherical images with HDR. The derivation required factors were obtained in the laboratory through measurements with a reflection plaque and a calibrated incandescent lamp. The sky luminance from the CCD spectroradiometer and camera-based luminance deviate by less than 20% for solar zenith angles less than 80° for all sky conditions. In addition, the measurement of the luxmeter and the camera-based global illuminance gave consistent results. Although the validation has not yet been performed over longer times (e.g., over 1 yr) or other locations, the HSI system has proven its potential for the measurement of both luminance and illuminance under a variety of meteorological conditions. This can be considered as a valuable achievement, because many other commercial photometric instruments measuring luminance are either costly or slow.

References

1. Commission International de l'Éclairage (CIE), *Daylight* (CIE Central Bureau Paris, 1970).
2. E. Vartiainen, "Electricity benefits of daylighting and photovoltaics for various solar facade layouts in office buildings," Energy Build. **33**, 113–120 (2001).
3. I. H. Yang and E. J. Nam, "Economic analysis of the daylight-linked lighting control system in office buildings," Solar Energy **84**, 1513–1525 (2010).
4. L. Heschong, "Daylighting and human performance," ASHRAE J. **44**, 65–67 (2002).
5. W. J. M. Van Bommel and G. J. Van den Beld, "Lighting for work: a review of visual and biological effects," Lighting Res. Technol. **36**, 255–269 (2004).
6. M. Hietanen, "Ocular exposure to solar ultraviolet and visible radiation at high latitudes," Scand. J. Work Environ. Health **17**, 398–403 (1991).
7. Commission International de l'Éclairage (CIE), *Photometry—the CIE System of Physical Photometry* (CIE Central Bureau Vienna, 2000).
8. V. Ferraro, M. Mele, and V. Malinelli, "Sky luminance measurements and comparison with models," J. Atmos. Sol.-Terr. Phys. **73**, 1780–1789 (2011).
9. R. Perez, R. Seals, and J. Michalsky, "All-weather model for sky luminance distribution—preliminary configuration and validation," Sol. Energy **50**, 235–245 (1993).
10. N. Igawa, Y. Koga, T. Matsuzawa, and H. Nakamura, "Models of sky radiance distribution and sky luminance distribution," Sol. Energy **77**, 137–157 (2004).
11. J. Krochmann and M. Seidl, "Quantitative data on daylight for illuminating engineering," Lighting Res. Technol. **6**, 165–171 (1974).
12. M. Karayel, M. Navvab, E. Ne'eman, and S. Selkowitz, "Zenith luminance and sky luminance distributions for daylighting calculations," Energy Build. **6**, 283–291 (1984).
13. S. Janjai, I. Masiri, M. Nunez, and J. Laksanaboonsong, "Modeling sky luminance using satellite data to classify sky conditions," Build. Environ. **43**, 2059–2073 (2008).
14. D. Kinghorn and T. Muneer, "All-sky zenith luminance models for the UK," Lighting Res. Technol. **31**, 49–56 (1999).
15. A. Cazorla, F. J. Olmo, and L. Alados-Arboledas, "Development of a sky imager for cloud cover assessment," J. Opt. Soc. Am. A **25**, 29–39 (2008).
16. J. E. Shields, R. W. Johnson, M. E. Karr, and J. L. Wertz, "Automated day/night whole sky imagers for field assessment of cloud cover distributions and radiance distribution," in *Tenth Symposium on Meteorological Observations and Instrument* (American Meteorological Society, 1998).
17. U. Feister, J. Shields, M. Karr, R. Johnson, K. Dehne, and M. Woldt, "Ground-based cloud images and sky radiance in the visible and near infrared region from whole sky image measurement," in *EUMETSAT Satellite Application Facility Workshop* (German Weather Service and World Meteorological Organization, 2000), pp. 79–88.

18. A. Kreuter, M. Zangerl, M. Schwarzmann, and M. Blumthaler, "All-sky imaging: a simple, versatile system for atmospheric research," Appl. Opt. **48**, 1091–1097 (2009).

19. M. Yamashita, M. Yoshimura, and T. Nakashizaka, "Cloud cover estimation using multitemporal hemispherical imageries," Int. Arch. Photogram. Rem. Sens. Spatial Inform. Sci. **35**, 826–829 (2004).

20. A. Heinle, A. Macke, and A. Srivastav, "Automatic cloud classification of whole sky images," Atmos. Meas. Tech. **3**, 557–567 (2010).

21. F. J. Olmo, A. Cazorla, L. Alados-Arboledas, M. A. López-Álvarez, J. Hernández-Andrés, and J. Romero, "Retrieval of the optical depth using an all-sky CCD camera," Appl. Opt. **47**, H182–H189 (2008).

22. K. J. Voss and G. Zibordi, "Radiometric and geometric calibration of a visible spectral electro-optic "fisheye" camera radiance distribution system," J. Atmos. Oceanic Technol. **6**, 652–662 (1989).

23. E. G. Rossini and A. Krenzinger, "Maps of sky relative radiance and luminance distributions acquired with a monochromatic CCD camera," Sol. Energy **81**, 1323–1332 (2007).

24. R. Román, M. Antón, A. Cazorla, A. de Miquel, F. J. Olmo, J. Bilbao, and L. Alados-Arboledas, "Calibration of an all-sky camera for obtaining sky radiance at three wavelengths," Atmos. Meas. Tech. **5**, 2013–2024 (2012).

25. G. G. Roy, S. Hayman, and W. Julian, "Sky modeling from digital imagery," ARC Project A89530177, Final Report (The University of Sydney and Murdoch University, 1998).

26. A. Ansko, K. Eerme, S. Lätt, M. Noorma, and U. Veismann, "Study of suitability of AvaSpec array spectrometer for solar UV field measurements," Atmos. Chem. Phys. **8**, 3247–3253 (2008).

27. N. Kouremeti, A. Bais, S. Kazadzis, M. Blumthaler, and R. Schmitt, "Charge-coupled device spectrograph for direct solar irradiance and sky radiance measurements," Appl. Opt. **47**, 1594–1607 (2008).

28. L. Ylianttila, R. Visuri, L. Huurto, and K. Jokela, "Evaluation of a single-monochromator diode array spectroradiometer for sunbed UV-radiation measurements," Photochem. Photobiol. **81**, 333–341 (2005).

29. A. Kreuter and M. Blumthaler, "Stray light correction for solar measurements using array spectrometers," Rev. Sci. Instrum. **80**, 096108 (2009).

30. G. Seckmeyer, A. Bais, G. Bernhard, M. Blumthaler, S. Drüke, P. Kiedron, K. Lantz, R. L. McKenzie, and S. Riechelmann, "Instruments to measure solar ultraviolet radiation, part 4: array spectroradiometers," in *WMO, Global Atmospheric Watch* (World Meteorological Organization, 2010), p. 43.

31. D. Pissulla, G. Seckmeyer, R. R. Cordero, M. Blumthaler, B. Schallhart, A. Webb, R. Kift, A. Smedley, A. F. Bais, N. Kouremeti, A. Cede, J. Herman, and M. Kowalewski, "Comparison of atmospheric spectral radiance measurement from five independently calibrated systems," Photochem. Photobiol. Sci. **8**, 516–527 (2009).

32. R. R. Cordero, G. Seckmeyer, D. Pissulla, and F. Labbe, "Uncertainty of experimental integrals: application to the UV index calculation," Metrologia **45**, 1–10 (2008).

33. S. Wuttke and G. Seckmeyer, "Spectral radiance and sky luminance in Antarctica: a case study," Theor. Appl. Climatol. **85**, 131–148 (2006).

34. S. Wuttke, G. Bernhard, J. Ehramjian, R. McKenzie, P. Johnston, M. O'Neil, and G. Seckmeyer, "New spectroradiometers complying with NDSC standards," J. Atmos. Ocean. Technol. **23**, 241–251 (2006).

35. G. Bernhard and G. Seckmeyer, "Uncertainty of measurements of spectral solar UV irradiance," J. Geophys. Res. **104**, 14321–14345 (1999).

36. R. R. Cordero, G. Seckmeyer, D. Pissulla, and F. Labbe, "Uncertainty evaluation of spectral UV irradiance measurements," Meas. Sci. Technol. **19**, 045104 (2008).

37. Commission International de l'Éclairage (CIE), *Characterization of the Performance of Illuminance Meters and Luminance Meters* (CIE Central Bureau Vienna, 2012).

38. Commission International de l'Éclairage (CIE), *International Lighting Vocabulary* (CIE Central Bureau Vienna, 2011).

39. Czibula & Grundmann, "*Photometer Datasheet,*" (Czibula & Grundmann GmbH, 2006).

40. D. Schneider, E. Schwalbe, and H. G. Maas, "Validation of geometric models for fisheye lenses," ISPRS J. Photogramm. Remote Sens. **64**, 259–266 (2009).

41. M. Gates, ed., www.stellarium.org/de (2009).

42. M. A. Robertson, S. Borman, and R. L. Stevenson, "Estimation-theoretic approach to dynamic range enhancement using multi exposures," J. Electron. Imaging **12**, 219–228 (2003).

43. N. Sun, H. Mansour, and R. Ward, "HDR image construction from multi-exposed stereo LDR images," in *Proceedings of IEEE 17th International Conference on Image Processing* (IEEE, 2010), pp. 2973–2976.

44. DIN 5032, *International Vocabulary of Basic and General Terms in Metrology* (Beuth, 1999).

45. P. R. Tregenza and I. M. Waters, "Daylight coefficients," Lighting Res. Technol. **15**, 65–71 (1983).

46. P. J. Starks, E. A. Walter-Shea, F. R. Schiebe, and B. L. Markham, "Temperature sensitivity characterization of a silicon diode array spectroradiometer," Remote Sens. Environ. **51**, 385–389 (1995).

47. J. Estrada, R. Alvarez, T. Abbott, J. Annis, M. Bonati, E. Buckley-Geer, J. Campa, H. Cease, S. Chappa, D. Depoy, G. Derylo, H. T. Diehl, B. Flaugher, J. Hao, S. Holland, D. Huffman, I. Karliner, D. Kubik, S. Kuhlmann, K. Kuk, H. Lin, N. Roe, V. Scarpine, R. Schmidt, K. Schultz, T. Shaw, V. Simaitis, H. Spinka, W. Stuermer, D. Tucker, A. Walker, and W. Wester, "Focal plane detectors for dark energy camera (DECam)," Proc. SPIE **7735**, 77351R (2010).